Anisotropic Energy Transfer and Conversion in Magnetized Compressible Turbulence

Du, Senbei
Li, Hui
Fu, Xiangrong
Gan, Zhaoming

To be published in: The Astrophysical Journal

DOI to publisher's version: 10.3847/1538-4357/acc5e9

The Astrophysical Journal, 948:72 (11pp), 2023 May 10 https://doi.org/10.3847/1538-4357/acc5e9

Anisotropic Energy Transfer and Conversion in Magnetized Compressible Turbulence

Senbei Du[1], Hui Li[1], Xiangrong Fu[2], and Zhaoming Gan[2]
[1] Los Alamos National Laboratory, Los Alamos, NM 87545, USA
[2] New Mexico Consortium, Los Alamos, NM 87544, USA
Received 2023 February 4; revised 2023 March 15; accepted 2023 March 18; published 2023 May 9

Abstract

We present a spatial filtering (or coarse-graining) analysis on 3D magnetized magnetohydrodynamic (MHD) turbulence simulations. The filtered compressible MHD formulae show transfer of kinetic and magnetic energies from large to small scales, as well as energy conversion between kinetic, magnetic, and thermal energies. The anisotropic filtering enables separate analyses of the energy flows perpendicular and parallel to the global mean magnetic field. Anisotropy in energy cascade is demonstrated by the larger perpendicular energy cascade rate and also the larger perpendicular wavenumbers associated with the peak energy transfer rate. We also find that the "inertial range" along the parallel (perpendicular) direction in the anisotropic energy cascade formulation is no longer strictly dissipation-free, because it includes the dissipation in the perpendicular (parallel) direction. A change in the driving force (kinetic only versus kinetic and magnetic) affects the energy conversion between kinetic and magnetic energies. While the compressibility of the driving force changes the partition of different channels of energy transfer and conversion, and also increases the total energy transfer rate, the global energy flow remains unaffected by compressibility qualitatively. Our analysis can be applied to multispacecraft observations of turbulence in the solar wind or a planetary magnetosphere.

Unified Astronomy Thesaurus concepts: Solar wind (1534); Interplanetary turbulence (830); Space plasmas (1544); Magnetohydrodynamics (1964)

1. Introduction

It is well established that homogeneous incompressible hydrodynamic turbulence possesses an inertial range of scales where the cross-scale energy transfer rate is a constant (Kolmogorov 1991). Within the inertial range, kinetic energy is transferred conservatively from large to small scales at a scale-independent rate. The situation is more complicated for magnetized plasmas, which tend to be highly anisotropic with respect to the mean magnetic field. Magnetohydrodynamics (MHD) is a common framework to study plasma turbulence. Bian & Aluie (2019) suggest that, in incompressible MHD, the sum of kinetic and magnetic energy cascades through the "inertial–inductive" scales. Depending on the nature of the driving force, kinetic energy can be converted to magnetic energy or vice versa (Bian & Aluie 2019; Yang et al. 2021). For compressible hydrodynamic or MHD turbulence, kinetic energy can be converted to thermal energy due to pressure dilatation (Yang et al. 2016). Compressibility also introduces additional terms for the cross-scale energy cascade (Aluie et al. 2012; Aluie 2013) and energy conversion between kinetic and magnetic energies (Du et al. 2022).

In this paper, we use compressible MHD simulations to study anisotropic turbulence. We use an anisotropic filtering method to analyze the cross-scale energy transfer and conversion between different energies. Spatial filtering (or coarse-graining) is a powerful technique as it allows quantitative identification of various energy transfer and conversion terms (Aluie et al. 2012; Aluie 2013; Yang et al. 2016; Bian & Aluie 2019). In general, the cross-scale energy transfer rate is consistent with estimates from third-order laws of structure functions (Kolmogorov 1991; Politano & Pouquet 1998; Banerjee & Galtier 2013; Yang et al. 2022). However, most previous analyses of MHD turbulence based on the filtering approach have not considered the effects of anisotropy due to background magnetic field, and related simulations (Yang et al. 2016, 2021; Bian & Aluie 2019) are based on weakly magnetized plasmas so that the turbulence therein is approximately isotropic. In many typical space, astrophysical, and laboratory plasmas, a background magnetic field is present, making turbulence highly anisotropic. Theories and simulations suggest that in the presence of a guiding magnetic field, the nonlinear interaction between Alfvén waves and nonpropagating "nearly incompressible" modes is important (Shebalin et al. 1983; Zank & Matthaeus 1992, 1993; Oughton et al. 1994; Montgomery & Matthaeus 1995; Ng & Bhattacharjee 1996). Furthermore, the theory of weak turbulence was developed based on the absence of cascade parallel to the background magnetic field (Galtier et al. 2000). Alfvén waves propagating along the magnetic field also play a role in the energy transfer (Kraichnan 1965). For example, the "critical balance" model suggests that cross-scale energy transfer is due to interacting Alfvén wave packets, resulting in a scale-dependent anisotropy $k_{\parallel} \sim k_{\perp}^{2/3}$ (Goldreich & Sridhar 1995; Cho & Vishniac 2000). Regardless of the energy transfer mechanisms, it is clear that an isotropic filtering approach is not appropriate for studying anisotropic plasma turbulence. The work presented in this paper will address this problem by considering an anisotropic filtering method. A recent work discusses the anisotropic cascade with the filtering method (Manzini et al. 2022b), using decaying Hall MHD simulations. An anisotropic distribution of cascade rate in the parallel–perpendicular plane is illustrated when a background magnetic field is present.

Turbulence energy cascade has also been investigated using space plasma observations. The energy cascade rate can be

estimated from single-spacecraft observations based on the third-order law (Sorriso-Valvo et al. 2007; Hadid et al. 2018; Andrés et al. 2021). A common issue for such observations is that the cascade rate can only be calculated along the sampling trajectory, while the third-order laws are derived for isotropic turbulence. Taylor et al. (2003) show in simulations that the cascade rate calculated along different directions can vary wildly, even in isotropic hydrodynamic turbulence simulations. Careful directional averaging is needed to recover the isotropic cascade rate, and this poses a challenge for spacecraft observations. The filtering method requires the evaluation of spatial gradients, so that multispacecraft observations such as those by Cluster, Magnetospheric Multiscale, and the future HelioSwarm (Klein et al. 2019) are needed for its application. This has been recently attempted by Manzini et al. (2022a), though with the caveat that the direction of filtering is limited to the spacecraft trajectories.

The primary purpose of this paper is to develop the formulation of the anisotropic spatial filtering method (Section 2), and to present the results on anisotropic cascades using compressible MHD turbulence simulations (Section 3). Discussions and conclusions are summarized in Section 4.

2. Method and Expectations

2.1. Spatial Filtering

The basic idea of spatial filtering is to derive the scale-dependent energy equations. The spatial filtering operation is defined as the convolution between a field quantity $A(\boldsymbol{x})$ and a filtering kernel $G_l(\boldsymbol{r})$ that depends on the scale l, i.e.,

$$\bar{A}_l(\boldsymbol{x}) = \int A(\boldsymbol{x}+\boldsymbol{r}) G_l(\boldsymbol{r}) d^3r. \tag{1}$$

For simplicity, the filtering kernel G_l can be chosen to be a boxcar function, i.e., $G_l(\boldsymbol{r}) = \text{const}$ for $|\boldsymbol{r}| \leqslant l$ and $G_l(\boldsymbol{r}) = 0$ elsewhere (Yang et al. 2016; Matthaeus et al. 2020). The result of the spatial filtering $\bar{A}_l$ is a low-pass-filtered field of the original quantity A. Other choices such as a Gaussian or sharp spectral filter have also been used in previous studies (Yang et al. 2021). The boxcar function is used in this work, and we have verified that using a sharp spectral filter will result in a better defined inertial range but does not change the results qualitatively. More theoretical aspects of the filtering approach can be found in previous publications by, e.g., Germano (1992), Eyink (2005), and Aluie (2013). In compressible turbulence where the density is not a constant, it is convenient to introduce a density-weighted average, also known as the Favre average (Favre 1992), defined as

$$\tilde{A}_l(\boldsymbol{x}) = \overline{\rho A}/\bar{\rho}, \tag{2}$$

where ρ is the plasma mass density. As discussed by Aluie (2013), the density-weighted average has the nice property of satisfying the inviscid criterion, meaning that the viscous contribution to the momentum and energy equations vanishes in the limit of small viscosity and large length scale. By applying the spatial filtering to the ideal MHD momentum and energy equations, one can derive the low-pass-filtered energy equations for the kinetic and magnetic energy densities. The equations are listed as follows (the subscript l is neglected for simplicity of notation):

$$\frac{\partial}{\partial t}\left(\frac{1}{2}\bar{\rho}|\tilde{\boldsymbol{u}}|^2\right) + \nabla\cdot\boldsymbol{j} = -\Pi^u - Q^{ut} + \Phi^{bu}, \tag{3}$$

$$\frac{\partial}{\partial t}\left(\frac{|\overline{\boldsymbol{B}}|^2}{8\pi}\right) + \nabla\cdot\boldsymbol{S} = -\Pi^b - \Phi^{bu}. \tag{4}$$

Following the conventional notation, $\boldsymbol{u}$ and $\boldsymbol{B}$ are the plasma bulk velocity and magnetic field, respectively. The large-scale kinetic and magnetic energy densities are defined as $\bar{\rho}|\tilde{\boldsymbol{u}}|^2/2$ and $|\overline{\boldsymbol{B}}|^2/8\pi$ (we use Gaussian units for the equations). The divergence terms $\nabla\cdot\boldsymbol{j}$ and $\nabla\cdot\boldsymbol{S}$ represent spatial transport of energy, and they are not of particular interest for this work. The Π^u and Π^b terms represent the rate of cross-scale energy transfer for kinetic and magnetic energies, respectively. These are presented as sinks in the energy equations, meaning that a transfer of energy from large to small scales follows from positive Π terms. The term Φ^{bu} represents the energy conversion from magnetic to kinetic energy because the same term with opposite signs appears in both kinetic and magnetic energy equations. Finally, the term Q^{ut} represents the conversion from kinetic energy to thermal energy due to compression (also known as pressure dilatation). The various terms in Equations (3) and (4) are expanded as follows:

$$\boldsymbol{j} = \frac{1}{2}\bar{\rho}\,|\tilde{\boldsymbol{u}}|^2\tilde{\boldsymbol{u}} + \bar{\rho}\tilde{\boldsymbol{\tau}}_{uu}\cdot\tilde{\boldsymbol{u}} - \frac{\overline{\boldsymbol{\tau}}_{BB}}{4\pi}\cdot\tilde{\boldsymbol{u}} + \frac{\bar{\tau}_{BB}}{8\pi}\tilde{\boldsymbol{u}} - \frac{\overline{\boldsymbol{u}}\times\overline{\boldsymbol{B}}}{4\pi}\times\overline{\boldsymbol{B}} + \bar{p}\,\overline{\boldsymbol{u}}; \tag{5}$$

$$\boldsymbol{S} = \frac{c}{4\pi}\overline{\boldsymbol{E}}\times\overline{\boldsymbol{B}} + \frac{\overline{\boldsymbol{u}}\times\overline{\boldsymbol{B}}}{4\pi}\times\overline{\boldsymbol{B}} = -\frac{\overline{\boldsymbol{\tau}}_{u\times B}}{4\pi}\times\overline{\boldsymbol{B}}; \tag{6}$$

$$\Pi^u = -\bar{\rho}\tilde{\boldsymbol{\tau}}_{uu}\colon\nabla\tilde{\boldsymbol{u}} + \frac{\overline{\boldsymbol{\tau}}_{\rho u}\cdot\nabla\bar{p}}{\bar{\rho}} + \frac{\overline{\boldsymbol{\tau}}_{BB}}{4\pi}\colon\nabla\tilde{\boldsymbol{u}} - \frac{\bar{\tau}_{BB}}{8\pi}\nabla\cdot\tilde{\boldsymbol{u}} + \frac{\overline{\boldsymbol{\tau}}_{\rho u}\cdot(\nabla\bar{B}^2/2 - \nabla\cdot\overline{\boldsymbol{B}}\,\overline{\boldsymbol{B}})}{4\pi\bar{\rho}} \tag{7}$$

$$\Pi^b = -\frac{c\overline{\nabla\times\boldsymbol{B}}}{4\pi}\cdot\frac{\overline{\boldsymbol{\tau}}_{u\times B}}{c} \tag{8}$$

$$\Phi^{bu} = \Phi^{bu}_1 + \Phi^{bu}_2 = -\frac{\overline{\boldsymbol{B}}\,\overline{\boldsymbol{B}}}{4\pi}\colon\nabla\overline{\boldsymbol{u}} + \frac{\bar{B}^2}{8\pi}(\nabla\cdot\overline{\boldsymbol{u}}) \tag{9}$$

$$Q^{ut} = -\bar{p}\nabla\cdot\overline{\boldsymbol{u}}. \tag{10}$$

The τ terms are Reynolds stress-like terms, i.e., $\bar{\tau}_{fg} = \overline{fg} - \bar{f}\,\bar{g}$ and $\tilde{\tau}_{fg} = \widetilde{fg} - \tilde{f}\,\tilde{g}$. More explicitly, we have

$$\tilde{\boldsymbol{\tau}}_{uu} = \widetilde{\boldsymbol{u}\boldsymbol{u}} - \tilde{\boldsymbol{u}}\tilde{\boldsymbol{u}}; \quad \overline{\boldsymbol{\tau}}_{BB} = \overline{\boldsymbol{B}\boldsymbol{B}} - \overline{\boldsymbol{B}}\,\overline{\boldsymbol{B}}; \quad \bar{\tau}_{BB} = \overline{B^2} - \bar{B}^2;$$
$$\overline{\boldsymbol{\tau}}_{\rho u} = \overline{\rho\boldsymbol{u}} - \bar{\rho}\,\overline{\boldsymbol{u}} = \bar{\rho}(\tilde{\boldsymbol{u}} - \overline{\boldsymbol{u}}); \quad \overline{\boldsymbol{\tau}}_{u\times B} = \overline{\boldsymbol{u}\times\boldsymbol{B}} - \overline{\boldsymbol{u}}\times\overline{\boldsymbol{B}}.$$

We note that $\tilde{\boldsymbol{\tau}}_{uu}$ and $\overline{\boldsymbol{\tau}}_{BB}$ are second-rank tensors, $\overline{\boldsymbol{\tau}}_{\rho u}$ and $\overline{\boldsymbol{\tau}}_{u\times B}$ are vectors, and $\bar{\tau}_{BB}$ is a scalar. The colon symbol denotes the double contraction between two second-rank tensors. We emphasize that the energy conversion terms Φ^{bu} and Q^{ut} do not exist in incompressible neutral fluid, but they can be important for compressible MHD. It is known that kinetic energy is an inviscid invariant in incompressible hydrodynamics. Compressible MHD contains the conversion between kinetic, magnetic, and thermal energy, so that only the total energy (but not each individual energy component) is an ideal invariant. Bian &

Aluie (2019) consider incompressible MHD turbulence, where it is found that the total transfer flux of kinetic and magnetic energies is approximately constant in the inertial range, while the energy conversion between the two plays an important role especially at large scales. We also note that, unlike the cross-scale energy transfer terms Π^u and Π^b, the terms Φ^{bu} and Q^{ut} do not involve sub-scale fields, and they describe the energy conversion at large scales only, as suggested by Equations (3) and (4) for the low-pass-filtered energies.

As mentioned earlier, most previous studies assume an isotropic filtering kernel, i.e., $G_l(\boldsymbol{r}) = G_l(r)$. A useful property of isotropic filtering is that the filtering operation commutes with the temporal and spatial derivatives. In this work, we consider anisotropic filtering in magnetized plasmas with approximately 2D and 1D symmetries with respect to the background magnetic field. We introduce the perpendicular and parallel filtering operators

$$\bar{A}^{\perp}(\boldsymbol{x}) = \int A(\boldsymbol{x} + \boldsymbol{r}_{\perp}) G_{\perp}(\boldsymbol{r}_{\perp}) d\boldsymbol{r}_{\perp};$$
$$\bar{A}^{\parallel}(\boldsymbol{x}) = \int A(\boldsymbol{x} + \boldsymbol{r}_{\parallel}) G_{\parallel}(\boldsymbol{r}_{\parallel}) d\boldsymbol{r}_{\parallel}. \quad (11)$$

It can be shown that both operators commute with spatial derivatives, under the same condition for the commutation of 3D isotropic filter. Correspondingly, the Favre averaging can also be redefined as $\tilde{A}^{\perp}$, $\tilde{A}^{\parallel}$, and so can the Reynolds stress-like terms. It follows that the filtered energy equations remain the same formally; we only need to replace all the filtering operators with perpendicular or parallel filtering operators. The perpendicular and parallel wavenumbers will also be used in this paper, and they are defined as $k_{\perp} = 2\pi/l_{\perp}$ and $k_{\parallel} = 2\pi/l_{\parallel}$, where $l_{\perp}$ and $l_{\parallel}$ are the perpendicular and parallel filtering scales. In simulations, the useful range of wavenumber is limited by the box size L and the spatial resolution Δ, i.e., $2\pi/L_{\perp,\parallel} \leqslant k_{\perp,\parallel} \leqslant 2\pi/\Delta_{\perp,\parallel}$.

2.2. The Role of Dissipation in Anisotropic Turbulence

The analysis in the previous section uses the ideal MHD equations without explicit dissipation terms. Here, we show that the analysis based on anisotropic filtering (or spectral analysis in general) is affected by energy dissipation, even if one considers the inertial range only. A subtlety with the anisotropic filtering is that the perpendicular low-pass-filtered energy includes contributions from all parallel scales, and the parallel low-pass-filtered energy includes contributions from all perpendicular scales. This means that energy dissipation occurring at large $k_{\perp}$ (or $k_{\parallel}$) can affect the calculation of the parallel (or perpendicular) spectrum. For completeness, the dissipation terms can be added to the filtered equations. For simple viscous and ohmic dissipations that are employed in our simulations, these terms are

$$D_{\nu} = -(\nabla \cdot \overline{\boldsymbol{\Pi}}) \cdot \tilde{\boldsymbol{u}}; \quad D_{\eta} = -\eta \nabla^2 \overline{\boldsymbol{B}} \cdot \overline{\boldsymbol{B}}, \quad (12)$$

with the viscous stress tensor

$$\boldsymbol{\Pi} = \rho\nu\left(\nabla \boldsymbol{u} + \nabla \boldsymbol{u}^T - \frac{2}{3}(\nabla \cdot \boldsymbol{u})\boldsymbol{I}\right), \quad (13)$$

where ν and η are the coefficients of viscosity and resistivity, respectively; the superscript ^{T} denotes the transpose operation; and $\boldsymbol{I}$ is the identity tensor ($-D_{\nu}$ and $-D_{\eta}$ are added to the right-hand side of (3) and (4)). In incompressible fluids, the viscous dissipation term reduces to the same form as the ohmic dissipation, $D_{\nu} = -\rho\nu\nabla^2\bar{\boldsymbol{u}} \cdot \bar{\boldsymbol{u}}$.

For anisotropic MHD turbulence, we expect that the onset of dissipation occurs at a larger perpendicular scale than the parallel scale. This is seen by the following estimate. The perpendicular dissipation scale is found by equating the nonlinear eddy turnover time and the diffusive time using dimensional analysis, i.e., $(k_{\perp}\delta u)^{-1} = k_{\perp}^{-2}\nu^{-1}$. Further analysis yields the Kolmogorov dissipation scale $d = \nu^{3/4}\varepsilon^{-1/4}$ or wavenumber $k_{\mathrm{diss},\perp} = \nu^{-3/4}\varepsilon^{1/4}$, where ε is the energy cascade rate in the inertial range. For the parallel dissipation scale, since the Alfvén wave is the dominant physical process at large $k_{\parallel}$, we equate the Alfvén timescale and the diffusion timescale, so that $(k_{\parallel}V_{\mathrm{A}})^{-1} = k_{\parallel}^{-2}\nu^{-1}$. This yields $k_{\mathrm{diss},\parallel} = V_{\mathrm{A}}/\nu$ as the parallel dissipation wavenumber. Since δu at the dissipation scale ($=\nu^{1/4}\varepsilon^{1/4}$) is typically smaller than V_{A}, we would expect $k_{\mathrm{diss},\parallel} > k_{\mathrm{diss},\perp}$. The above discussion leads to the diagram illustrated in Figure 1, where the wavevector $k_{\parallel}$–$k_{\perp}$ space is divided into several regimes bounded by the solid black lines. The energy injection occurs at the largest scales, or smallest wavenumbers, at the bottom left corner of the diagram. In the inertial range, cross-scale energy transfer occurs in both parallel and perpendicular directions. The inertial range is divided into two regimes: one dominated by nonlinear perpendicular cascade and one dominated by the Alfvén wave, the former of which may be viewed as quasi-2D-like turbulence as it occupies the large-$k_{\perp}$ part of the wavevector space. The boundary between the nonlinear and Alfvén regimes is known as the critical balance curve. Here, we plot the classic model by Goldreich & Sridhar (1995), $k_{\parallel} = k_{\perp}^{2/3}\varepsilon^{1/3}/V_{\mathrm{A}}$, though we acknowledge that the exact shape of the critical balance curve is still controversial (Chhiber et al. 2020; Oughton & Matthaeus 2020). For the region with $k_{\perp} > k_{\mathrm{diss},\perp}$ and $k_{\parallel} < k_{\mathrm{diss},\parallel}$, we identify a new physical regime where the propagation of Alfvén waves competes with perpendicular dissipation. A boundary is found by equating the Alfvén timescale and the perpendicular diffusion timescale, which yields $k_{\parallel} = k_{\perp}^2\nu/V_{\mathrm{A}}$. Below the boundary, perpendicular dissipation is the dominant process that damps Alfvén waves. This boundary has rarely been discussed previously and we speculate the following reasons: (1) kinetic effects are likely important in this regime (e.g., Meyrand et al. 2016), so that the viscous dissipation timescale may not be relevant for applications; and (2) the entire region of $k_{\perp} > k_{\mathrm{diss},\perp}$ contains little power, so the boundary may not be energetically important. The analysis above uses viscous dissipation only, but the ohmic dissipation can be treated in the same way.

An interesting consequence of dissipation is that it affects the perpendicular and parallel cascade rates (Π terms) in the inertial range. The smaller dissipation wavenumber in the perpendicular direction suggests that perpendicular dissipation will be easier to resolve with numerical simulations. The fact is even more exaggerated by the use of an elongated grid along the parallel direction. This leads to a more suppressed parallel cascade rate $\Pi_{\parallel}$ compared to $\Pi_{\perp}$. Ideally, a simulation with adequate resolution would be able to see both perpendicular and parallel dissipation equally well. In such cases, it is not clear whether perpendicular or parallel dissipation would be stronger in magnitude. One may argue based on the theory of weak incompressible turbulence that the parallel cascade rate would still likely be suppressed (Galtier et al. 2000). We also

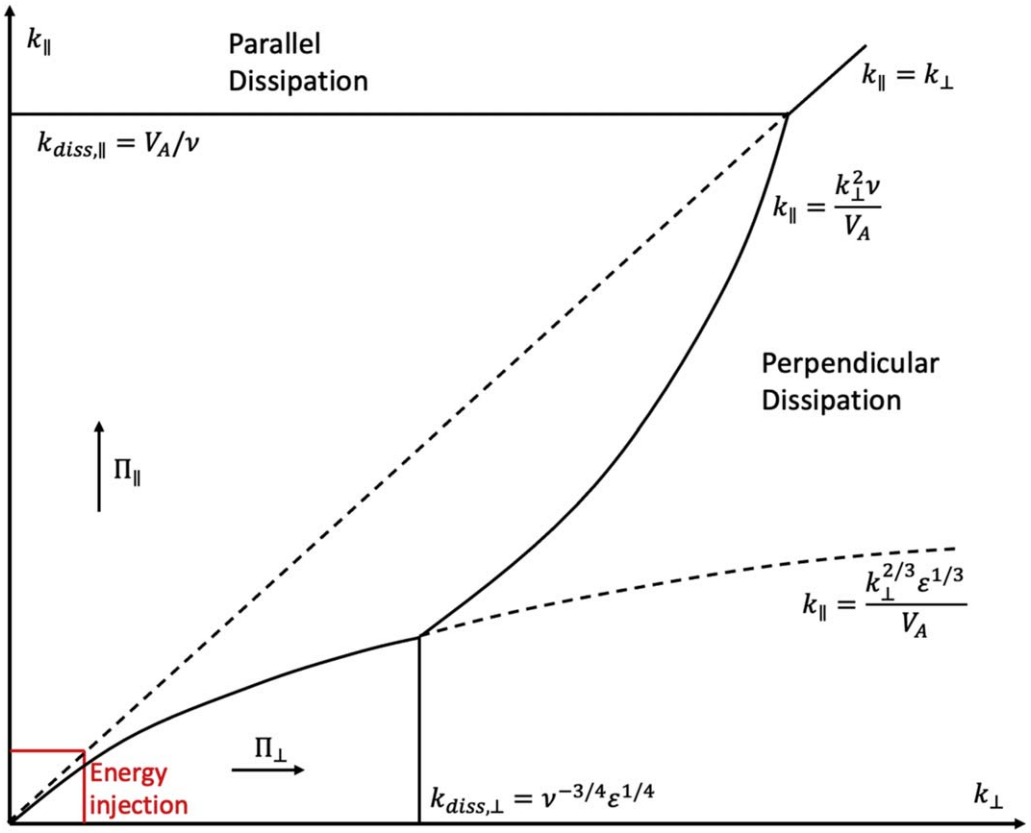

Figure 1. A diagram illustrating the role of dissipation in anisotropic turbulence.

note that the dissipation effects discussed here are not just an issue for grid-based numerical simulations. Actual in situ observations of turbulence could be subject to the same effects of dissipation because turbulence measurements are also reduced along the direction of spacecraft samples (e.g., Fredricks & Coroniti 1976). In such cases, the difference in measured perpendicular and parallel cascade rates may be an indicator of the actual dissipation mechanism.

3. Simulation Results

3.1. Description of Simulation Runs

We present 3D MHD simulation using the *Athena++* code (Stone et al. 2020), which solves the following sets of compressible MHD equations:

$$\frac{\partial \rho}{\partial t} + \nabla \cdot (\rho \boldsymbol{u}) = 0,$$

$$\frac{\partial \rho \boldsymbol{u}}{\partial t} + \nabla \cdot (\rho \boldsymbol{u}\boldsymbol{u} - \boldsymbol{B}\boldsymbol{B} + (p + B^2)\boldsymbol{I} - \boldsymbol{\Pi}) = 0,$$

$$\frac{\partial \boldsymbol{B}}{\partial t} - \nabla \times [(\boldsymbol{u} \times \boldsymbol{B}) - \eta(\nabla \times \boldsymbol{B})].$$

The viscous stress tensor $\boldsymbol{\Pi}$ is defined in Equation (13) in the previous section. An isothermal equation of state is used, i.e., $p = \rho c_s^2$, where the sound speed c_s is a constant. A background magnetic field B_0 is applied along the x-direction. Periodic boundary conditions are used for all three directions. Driving forces that follow an Ornstein–Uhlenbeck process can be applied to both velocity and magnetic field, following Gan et al. (2022). The amplitude of the driving force is specified by the parameters f_v for velocity and f_b for magnetic field. Energy injection is restricted to large-scale modes with wavelengths at least half the size of the perpendicular box. The driving force on velocity is decomposed as incompressible (solenoidal) and compressible (irrotational) components, i.e., $|\boldsymbol{f}_{v\parallel}| = |\boldsymbol{f}_{v\perp}| f_c/(1 - f_c)$, where f_c is a parameter characterizing the compressibility, and $\parallel$, $\perp$ are defined with respect to the wavevector $\boldsymbol{k}$. A purely compressible (incompressible) driving corresponds to $f_c = 1$ ($f_c = 0$).

Table 1
Summary of Simulation Runs

Run #	f_v	f_b	f_c	M_A	Re
0	0.0075	0	0	0.27	1.7×10^4
1	0.0075	0.0075	0	0.21	1.3×10^4
2	0.0075	0	0.9	0.24	1.5×10^4

To explore the effects of driving parameters on the results, we make three runs as summarized in Table 1. The varying parameters are the compressibility of driving as characterized by the parameter f_c, and types of driving (velocity only versus both velocity and magnetic field). For the base run R0, we consider incompressible driving $f_c = 0$ on velocity only. All three runs have a plasma beta (ratio between thermal pressure and magnetic pressure) $\beta = 1$. The viscosity and resistivity coefficients ν and η are set to be equal so that the magnetic Prandtl number is 1. The averaged Alfvén Mach number $M_A = \delta v_\perp / V_A$, where $\delta v_\perp = \sqrt{\langle \delta v_y^2 + \delta v_z^2 \rangle}$, during the steady-state phase of the simulation is listed in the table. The Reynolds

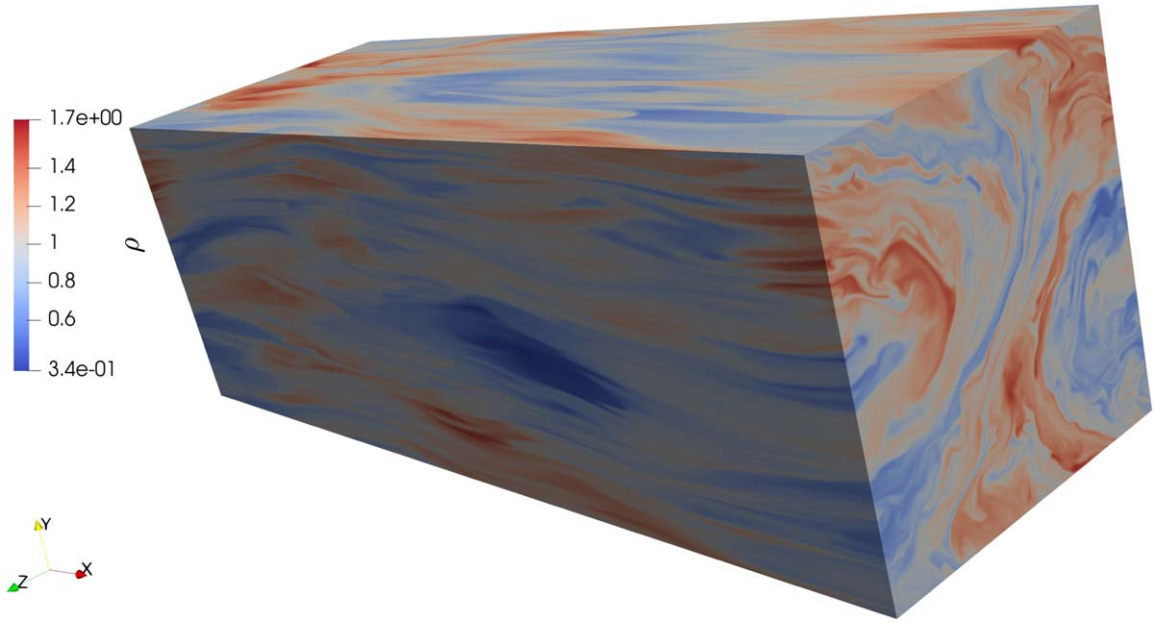

Figure 2. A snapshot of the 3D surface of the plasma density ρ for Run R0.

number is calculated as $Re = \delta v_\perp L_\perp/\nu$, where $L_\perp$ is the box size perpendicular to the mean magnetic field.

To save computational resources, all simulations use an elongated box $L_x = 3L_y = 3L_z$, and the number of cells ($256 \times 512 \times 512$) is reduced by half in the x-direction compared to the other two directions. The logic behind such a setup is the critical balance conjecture (Goldreich & Sridhar 1995), which suggests that the anisotropy of turbulent eddies is scale-dependent, following the relation $k_\perp/k_\parallel = (\delta v_\perp/V_A)^{-1}$, where turbulent velocity fluctuation follows a Kolmogorov-like scaling, $\delta v_\perp \propto k_\perp^{-1/3}$. Therefore, it is efficient to use an elongated simulation box along the mean magnetic field when turbulent Mach number M_A is smaller than 1. Critical balance also suggests that the anisotropy becomes even stronger at small scales, so a smaller number of cells are needed in the parallel direction (Beresnyak & Lazarian 2009). As discussed in Section 2, this setup is not ideal for resolving parallel dissipation. However, we argue that for practical applications in space plasmas, the physical dissipation mechanism is usually not fluid viscosity or resistivity; thus, resolving the parallel dissipation in MHD simulations seems like a lost cause and does not justify the extra computational cost associated with it.

Figure 2 shows a surface plot of plasma density from the simulation R0. The surface plot clearly demonstrates the anisotropic feature of turbulence as the simulation domain is filled by elongated structures. The time evolution of several box-averaged quantities is summarized in Figure 3. On the horizontal axis, the time t is normalized to the Alfvén time $\tau_A = L_x/V_A$. The top panel shows the turbulent Mach number and relative transverse magnetic fluctuations $\delta B_\perp/B_0$; the middle panel shows the relative density fluctuation $\delta\rho/\rho_0$ and the magnetic compressibility $\delta|\boldsymbol{B}|/|\delta\boldsymbol{B}|$ (ratio between magnetic field magnitude fluctuation and total magnetic field fluctuation); and the bottom panel shows the normalized cross-helicity $\sigma_c = 2\delta\boldsymbol{u}\cdot\delta\boldsymbol{B}/(\delta u^2 + \delta B^2)$ and residual energy $\sigma_r = (\delta u^2 - \delta B^2)/(\delta u^2 + \delta B^2)$.

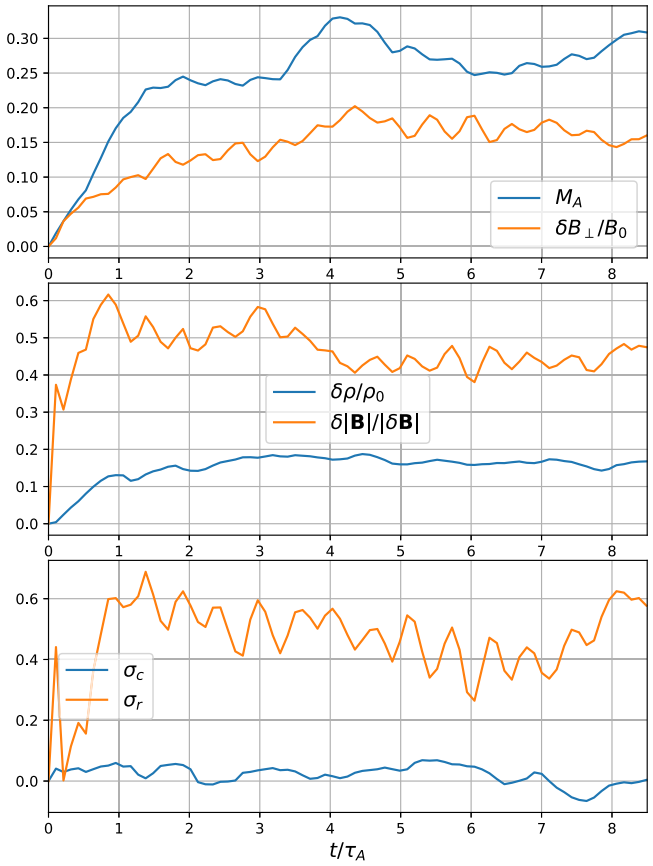

Figure 3. The time evolution of several box-averaged quantities.

The anisotropic Fourier power spectra of kinetic and magnetic fluctuations for Run R0 are shown in Figure 4, where the parallel and perpendicular reduced spectra are plotted as blue and orange curves, respectively. The solid and dashed lines represent velocity and magnetic spectra. The dotted line displays a $k^{-5/3}$ power law as a reference. The perpendicular and parallel power spectra ($P(k_\perp)$ and $P(k_\parallel)$) are calculated by

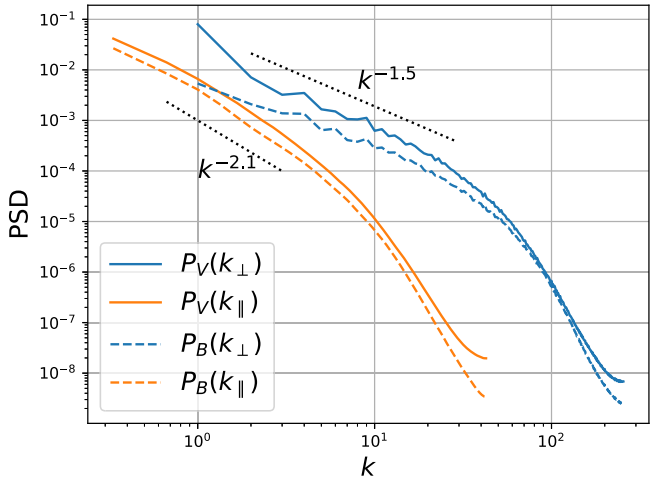

Figure 4. The anisotropic kinetic and magnetic power spectra for Run R0 at the end of the simulation.

reducing the 3D Fourier spectrum $P(\boldsymbol{k})$. Power-law spectra $k^{-1.5}$ and $k^{-2.1}$ are plotted as references, but we note that the differences between power-law indices of $-5/3$, $-3/2$, and -2 as suggested by different theoretical models (Kolmogorov 1991; Goldreich & Sridhar 1995; Boldyrev 2005) are minute and difficult to distinguish. At the same wavenumber ($k_\perp = k_\parallel$), the perpendicular power dominates over parallel power for both kinetic and magnetic fluctuations, which is expected for anisotropic MHD turbulence. The magnetic fluctuation level is lower than the kinetic fluctuation level, because the driving force is applied to velocity only for this run. An inertial range can be observed around $2 < k_\perp < 40$ where power-law spectra exist (at least for velocity). The parallel spectra roll over at a smaller wavenumber than the perpendicular spectra, while Figure 1 suggests that the onset of parallel dissipation should occur at a larger wavenumber. This suggests that perpendicular dissipation may be the dominant dissipation mechanism, affecting even the parallel spectra. The reason may be that (1) weakened parallel cascade leads to more energy flowing to the regime of perpendicular dissipation, or (2) the regime of parallel dissipation is underresolved due to limited numerical resolution.

3.2. Scale-dependent Energy Transfer and Conversion

Using the filtering method described in Section 2, we analyze the scale-dependent energy transfer and conversion rate in the simulations. Specifically, we study the terms Π^u, Π^b, Φ^{bu}, and Q^{ut} as functions of perpendicular and parallel wavenumbers. We find that these energy transfer and conversion rates can have significant fluctuations in time, even when the kinetic energy and magnetic energy appear to be stationary. These temporal variations can be dramatically reduced after averaging the rate over many saved data frames spanning more than an Alfvén time during the stationary stage of the evolution. For example, the results of Run R0 are averaged over 16 data frames during the later stage of the simulation (∼3 Alfvén times); further increasing the number of averaging steps does not change the results qualitatively.

Figure 5 shows the combinations of terms $\Pi^u + Q^{ut} - \Phi^{bu}$, $\Pi^b + \Phi^{bu}$, and $\Pi^u + \Pi^b + Q^{ut}$ as functions of the perpendicular and parallel wavenumbers. They represent the rate of change for the large-scale kinetic, magnetic, and total energy, respectively. Results for Run R0 are shown in the top panels. Although we do not see a wavenumber range where these terms are independent of scales, there is an intermediate range of scales where these terms are prominent, roughly corresponding to the inertial range of turbulence (see Figure 4). The perpendicular rate has a higher peak than the parallel one, which indicates weakened parallel cascade or the effect of dissipation as discussed in Section 2. Another possible reason is that the parallel rates are more affected by the injection range, which is $k \leqslant 2$ for both parallel and perpendicular wavenumbers. We note that the parallel and perpendicular rates are strictly equivalent at the highest wavenumber, where there is essentially no filtering. And the rate of change for total energy is small at the highest wavenumber, corresponding to a quasi-stationary state. The anisotropy is reflected in the different $k_\perp$ and $k_\parallel$ where the rates attain their peaks. It can be seen from the figure that the peaks of total rate $\Pi^u + \Pi^b + Q^{ut}$ correspond to $k_\perp \sim 5k_\parallel$, indicating a stronger perpendicular cascade that transfers energy to smaller perpendicular scales. Another feature is that while the kinetic energy flux $\Pi^u + Q^{ut} - \Phi^{bu}$ is positive, the magnetic energy flux $\Pi^b + \Phi^{bu}$ is negative. This is because the injected kinetic energy is being converted to magnetic energy, causing $\Phi^{bu} < 0$.

The same analysis is applied to Runs R1 and R2, and the results are shown in panels (c)–(f) of Figure 5. The behavior in wavevector anisotropy $k_\perp > k_\parallel$ is similar for these runs. The rate of change in magnetic energy is positive in Run R1, because of the large-scale driving in the magnetic field. Comparing Runs R0 and R2, we find that the compressibility of velocity driving does not affect the results qualitatively, but the peak rate of change becomes larger by a factor of ∼2 in the presence of compressible driving, as shown by the bottom panels of Figure 5.

In Figure 6, we decompose the kinetic-to-magnetic energy conversion into two terms Φ_1^{bu} and Φ_2^{bu} (see Equation (9)) for the three runs. The two terms Φ_1^{bu} and Φ_2^{bu} roughly represent the incompressible and compressible contributions to the energy conversion. The first term can be interpreted as processes of magnetic field-line stretching or tension release (Yang et al. 2016; Grete et al. 2021), and the second term as perpendicular expansion due to a magnetic pressure gradient (Du et al. 2022). For Run R0, panels (a) and (b) show that the incompressible contribution Φ_1^{bu} is negative and the compressible contribution Φ_2^{bu} is positive. The total energy conversion is mostly determined by the incompressible term, and is from kinetic to magnetic. The red curves in the figure represent the pressure dilatation Q^{ut}, which is positive, meaning kinetic energy is being converted to thermal energy. All these energy conversion terms behave similarly in perpendicular and parallel directions.

For Run R1 in panels (c) and (d), we find that Φ^{bu} is positive, so the magnetic energy is being converted to kinetic energy. This is because both kinetic and magnetic energies are injected at large scales. The overall contribution of the compressible term Φ_2^{bu} appears to dominate the energy conversion. The pressure dilatation behaves similarly to Run R0. The total magnetic-to-kinetic energy conversion in Run R2 is similar to that in R0, both having velocity driving only, as shown in panels (e) and (f) of Figure 6. The difference is that the energy conversion is dominated by the compressible term Φ_2^{bu} for Run R2 with a highly compressive driving force, while the energy conversion in Run R0 is dominated by the incompressible term Φ_1^{bu}. Therefore, the compressibility of driving does affect the

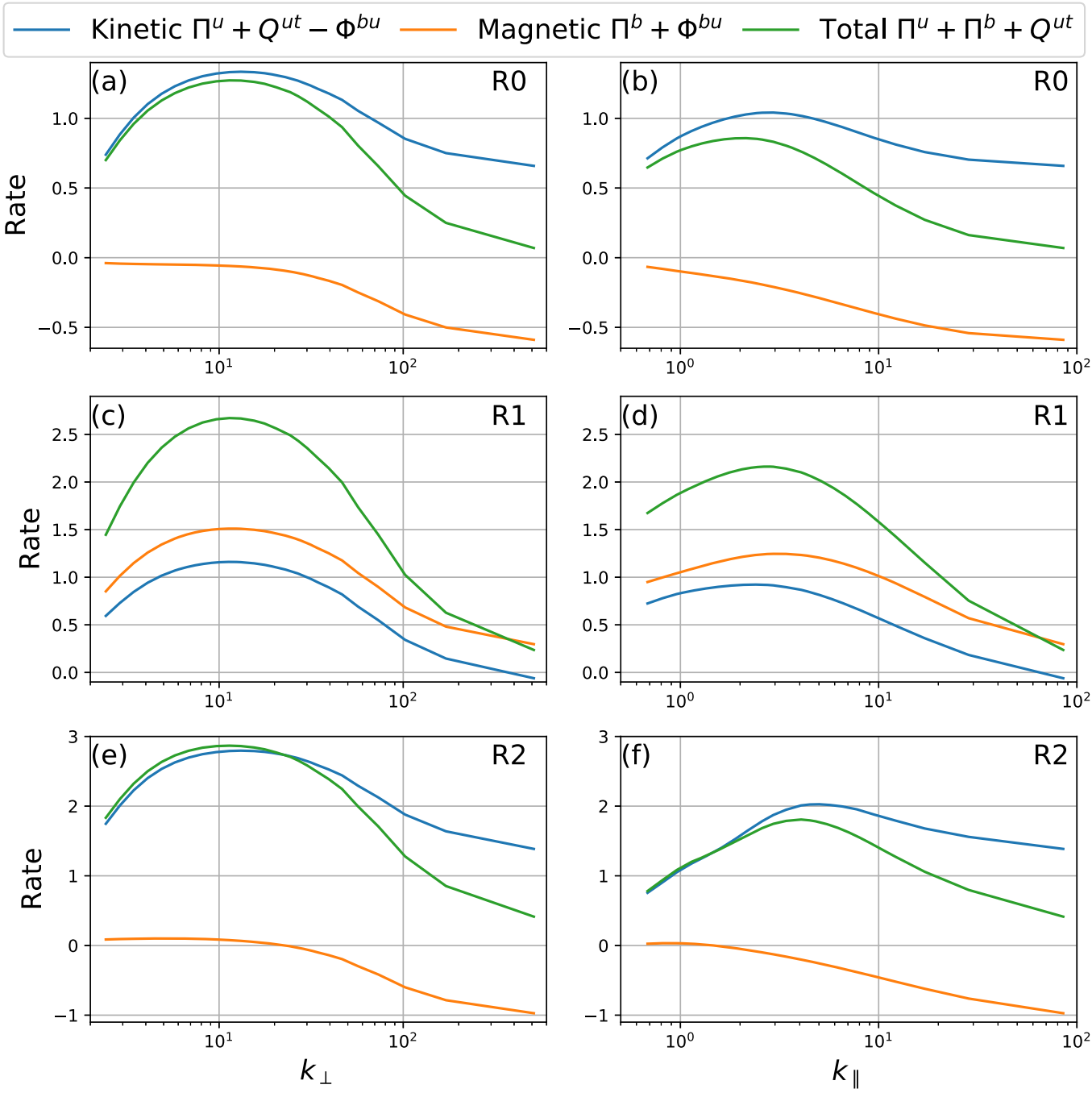

Figure 5. Scale-dependent rate of change for the volume-integrated kinetic (blue), magnetic (orange), and total (green) energy as functions of perpendicular (left) and parallel (right) wavenumbers for all three runs.

mechanism of energy conversion. The overall amplitudes of energy conversion rates, including the pressure dilatation, are also larger in the more compressible run R2.

Figure 7 shows the kinetic, magnetic, and total energy cascade rates Π^u, Π^b, and $\Pi^u + \Pi^b$ for Run R0. These are terms that represent the energy transfer through scales without changing the form of energy. They are no longer expected to be constant through the "inertial range" in compressible MHD, unlike the combinations shown in Figure 5. The horizontal dashed line denotes the total dissipation (heating) rate, which is the sum of the unfiltered pressure dilatation $-p\nabla\cdot\boldsymbol{u}$, viscous dissipation, and ohmic dissipation. Here, the viscous dissipation and ohmic dissipation are calculated from the formula $\boldsymbol{\Pi}$ $:\nabla\boldsymbol{u}+\eta\nabla\boldsymbol{B}:\nabla\boldsymbol{B}$, which can also be applied to the filtering analysis (see discussions in the next paragraph). In the fully developed incompressible turbulence, the energy cascade rate in the inertial range is expected to equal the dissipation rate (viscous and ohmic). For compressible turbulence, pressure dilatation can occur at large scales, resulting in an energy conversion range where the energy cascade rate is not a constant (Aluie et al. 2012). However, we still expect the peak total energy cascade rate to be comparable with the total dissipation rate (including pressure dilatation). Our results show a total dissipation rate that is reasonably consistent with the peak perpendicular energy cascade rate. The total dissipation rate is slightly smaller than the peak perpendicular

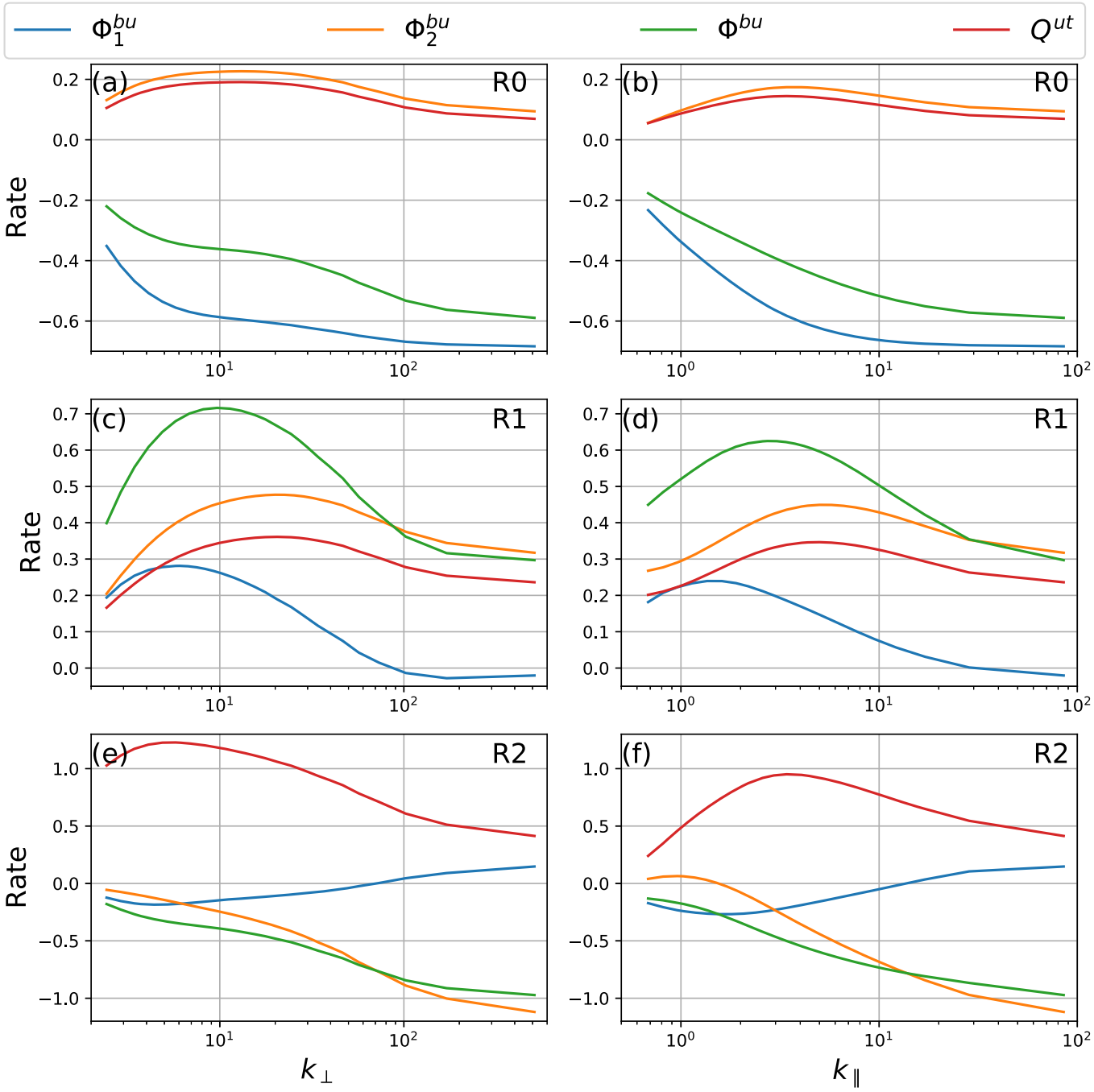

Figure 6. Scale-dependent conversion terms from magnetic to kinetic energy Φ^{bu} and from kinetic to thermal energy Q^{ut} as functions of perpendicular (left) and parallel (right) wavenumbers for all three runs.

cascade rate, which may be due to a small amount of numerical dissipation or errors. The peak parallel cascade rate is smaller, due to the property of weak turbulence or the effects of perpendicular dissipation or mixing of the energy injection range, similar to Figure 5.

The scale-dependent dissipation rate for Run R0 is shown in Figure 8. The rate is plotted as functions of perpendicular (blue) and parallel (orange) wavenumbers. Here, the dissipation rate is calculated with the first-order derivatives only, by

$$D = \overline{\mathbf{\Pi}}\colon \nabla\tilde{\boldsymbol{u}} + \eta\nabla\overline{\boldsymbol{B}}\colon \nabla\overline{\boldsymbol{B}} \tag{14}$$

instead of Equation (12), which uses the second-order derivatives. The two formulae are equivalent when integrated over the entire volume, given that the divergence term vanishes after integration due to the periodic boundary condition. It is seen that when calculated as a function of the perpendicular wavenumber, the dissipation rate is smaller than the rate evaluated at the same parallel wavenumber, consistent with our expectation discussed in Section 2. The figure confirms our speculation that the dissipation rate has a larger effect on the calculation of parallel cascade rate, leading to an apparently smaller parallel cascade rate than the perpendicular one in the inertial range. On the other hand, the results can also be interpreted as a natural consequence of weakened parallel energy cascade such as that of weak turbulence as less energy

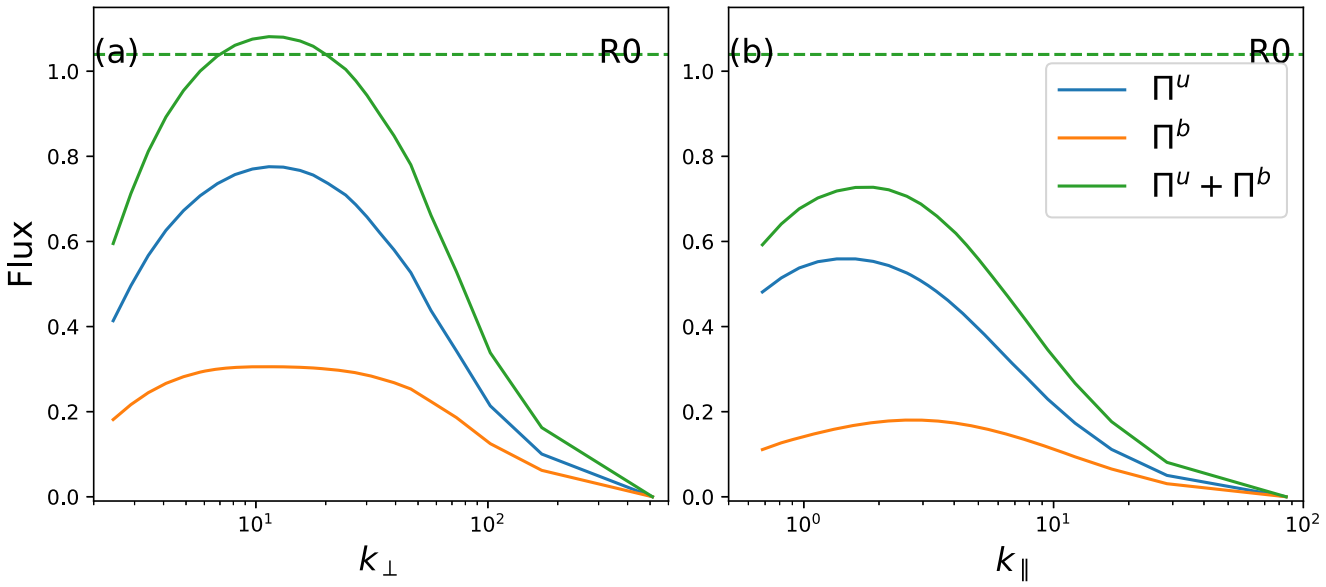

Figure 7. Scale-dependent energy cascade rates as functions of perpendicular (left) and parallel (right) wavenumbers for Run R0. The horizontal dashed line denotes the total heating rate.

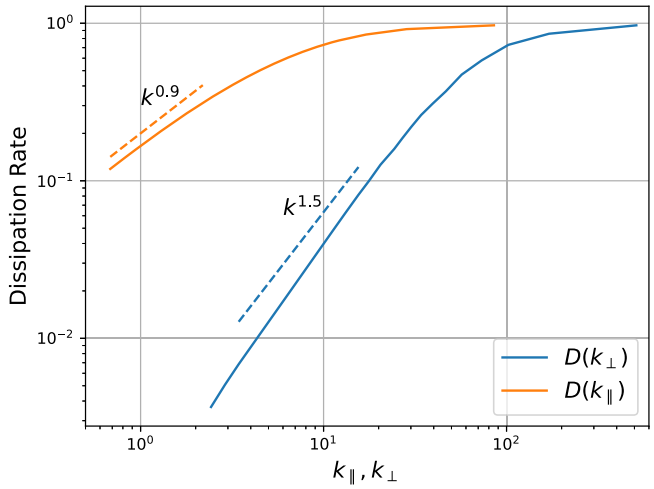

Figure 8. Scale-dependent dissipation rates as functions of the perpendicular (blue) and parallel (orange) wavenumbers for Run R0.

flows to the regime of parallel dissipation. At small $k_\perp$ or $k_\parallel$ that corresponds to the inertial range, the dissipation rates $D(k_\perp)$ and $D(k_\parallel)$ exhibit a power-law behavior. Dimensional analysis suggests that $D(k) \sim k^2 \delta u^2 \sim k^3 P(k)$ with $P(k)$ being the power spectrum. The power-law indices ($\sim$1.5 and 0.9) in Figure 8 correspond to spectral indices of ~ -1.5 and -2.1 for power spectra, which are visually consistent with Figure 4. One potential caveat is that Figure 4 plots standard Fourier spectra (equivalent to using a sharp spectral filter), which may not be exactly comparable with Figure 8, which uses a boxcar filter.

Figure 9 shows the decomposition of kinetic energy transfer into different terms as suggested by Equation (7). While Runs R0 and R1 are similar, the two pure hydrodynamic terms (blue and orange curves) are significantly stronger in R2. The orange curve is negative for all three runs, indicating that the energy transfer due to density variation (baropycnal work; Aluie 2013) counteracts the incompressible hydrodynamic contribution.

4. Discussions and Conclusions

We present 3D compressible MHD simulations of magnetized turbulence, and analyses of the energy transfer and conversion processes using a spatial filtering method. Here, anisotropic filtering operators are applied to directions parallel and perpendicular to the background magnetic field. Filtered MHD equations yield terms that represent the cross-scale kinetic and magnetic energy transfer, as well as conversion between different forms of energy (kinetic, magnetic, and thermal). The cross-scale energy transfer leads to the cascade of energy from large to small scales. Conversion between kinetic and magnetic energies is due to pressure dilatation, while conversion between magnetic and kinetic energies is due to magnetic field-line stretching and compression. Three simulation runs with different driving forces are performed, and the main results are summarized as follows.

1. The energy cascade is anisotropic with a stronger perpendicular cascade down to smaller scales. This is illustrated by the larger perpendicular wavenumbers associated with the peaks of the rate of change in large-scale energy (Figure 5).
2. The magnitude of the perpendicular cascade rate is larger than that of parallel cascade rate in our simulations (Figure 7). This could be explained by weak turbulence theory. Other possible reasons include the effect of underresolved parallel dissipation and the mixing of energy injection range and inertial range.
3. The compressibility of the driving force affects the mechanisms of energy transfer and conversion. The presence of compressible driving elevates the relative importance of terms related to pressure dilatation, baropycnal work, and compression of magnetic field. The overall energy flow does not change qualitatively with compressibility (comparing top and bottom panels in Figure 5), but we notice that the peak rates are larger in the more compressible run.
4. The direction of energy conversion depends on the driving force (Figure 6). As expected, energy conversion

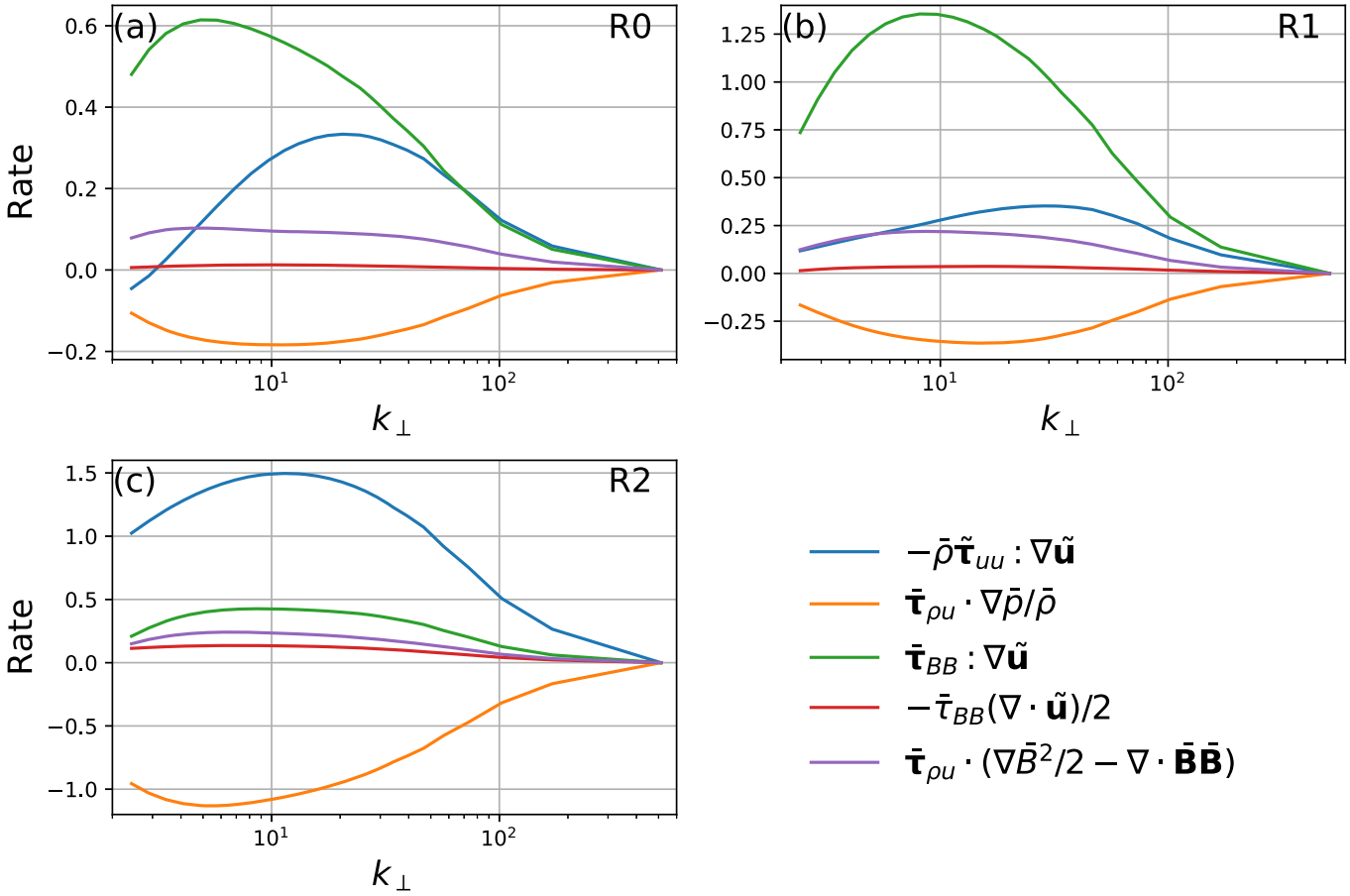

Figure 9. Scale-dependent energy transfer terms for kinetic energy as functions of the perpendicular wavenumber for all three runs.

from kinetic to magnetic energy occurs if only velocity is driven; and the reverse can occur if the driving force is also applied to the magnetic field.

Anisotropy is an important feature of magnetized plasma turbulence that is prevalent in many systems, and our analysis demonstrates the anisotropy in terms of turbulence energy cascade and conversion. The result of reduced parallel cascade rate is consistent with the theory of weak turbulence in incompressible MHD where parallel cascade is absent (Galtier et al. 2000), although our simulations are not exactly in the regime of the original theory. For strong turbulence, the anisotropic cascade rate is less understood theoretically (e.g., Beresnyak 2019; Schekochihin 2022). The anisotropy analysis can be applied to multispacecraft observations of heliospheric plasma turbulence (Manzini et al. 2022a).

We also identify a regime where the Alfvén waves are damped by perpendicular dissipation, as illustrated in Figure 1. We find that in viscous–resistive MHD turbulence, parallel dissipation occurs at a smaller scale than perpendicular dissipation. The new regime could provide the dominant dissipation mechanism of the Alfvénic turbulence, supported by the fact that the inertial range occurs at a smaller $k_\parallel$ range than the $k_\perp$ range. The anisotropic cascade rates in the inertial range may even serve as a probe to the physics of the dissipation mechanism in actual observations.

S.D. and H.L. acknowledge the support by DOE OFES program and LANL/LDRD program. X.F. and Z. G. are supported by NASA under Award No. 80NSSC20K0377. Useful discussions with W. Matthaeus, J. Steinberg, and Y. Yang are gratefully acknowledged. We also thank the anonymous referee for constructive comments. This research used resources provided by the Los Alamos National Laboratory Institutional Computing Program, which is supported by the U.S. Department of Energy National Nuclear Security Administration under Contract No. 89233218CNA000001.

ORCID iDs

Senbei Du https://orcid.org/0000-0003-1134-3909
Hui Li https://orcid.org/0000-0003-3556-6568
Xiangrong Fu https://orcid.org/0000-0002-4305-6624
Zhaoming Gan https://orcid.org/0000-0003-3886-0383

References

Aluie, H. 2013, PhyD, 247, 54
Aluie, H., Li, S., & Li, H. 2012, ApJL, 751, L29
Andrés, N., Sahraoui, F., Hadid, L., et al. 2021, ApJ, 919, 19
Banerjee, S., & Galtier, S. 2013, PhRvE, 87, 013019
Beresnyak, A. 2019, LRCA, 5, 2
Beresnyak, A., & Lazarian, A. 2009, ApJ, 702, 1190
Bian, X., & Aluie, H. 2019, PhRvL, 122, 135101
Boldyrev, S. 2005, ApJL, 626, L37
Chhiber, R., Matthaeus, W. H., Oughton, S., & Parashar, T. N. 2020, PhPl, 27, 062308
Cho, J., & Vishniac, E. T. 2000, ApJ, 539, 273
Du, S., Li, H., Fu, X., Gan, Z., & Li, S. 2022, ApJ, 925, 128
Eyink, G. L. 2005, PhyD, 207, 91

Favre, A. J. A. 1992, in Studies in Turbulence, ed. T. B. Gatski, C. G. Speziale, & S. Sarkar (New York, NY: Springer), 324
Fredricks, R., & Coroniti, F. 1976, JGR, 81, 5591
Galtier, S., Nazarenko, S., Newell, A. C., & Pouquet, A. 2000, JPlPh, 63, 447
Gan, Z., Li, H., Fu, X., & Du, S. 2022, ApJ, 926, 222
Germano, M. 1992, JFM, 238, 325
Goldreich, P., & Sridhar, S. 1995, ApJ, 438, 763
Grete, P., O'Shea, B. W., & Beckwith, K. 2021, ApJ, 909, 148
Hadid, L. Z., Sahraoui, F., Galtier, S., & Huang, S. 2018, PhRvL, 120, 055102
Klein, K., Alexandrova, O., Bookbinder, J., et al. 2019, arXiv:1903.05740
Kolmogorov, A. N. 1991, RSPSA, 434, 15
Kraichnan, R. H. 1965, PhFl, 8, 1385
Manzini, D., Sahraoui, F., & Califano, F. 2022a, arXiv:2208.00855
Manzini, D., Sahraoui, F., Califano, F., & Ferrand, R. 2022b, PhRvE, 106, 035202
Matthaeus, W. H., Yang, Y., Wan, M., et al. 2020, ApJ, 891, 101
Meyrand, R., Galtier, S., & Kiyani, K. H. 2016, PhRvL, 116, 105002
Montgomery, D., & Matthaeus, W. H. 1995, ApJ, 447, 706
Ng, C., & Bhattacharjee, A. 1996, ApJ, 465, 845
Oughton, S., & Matthaeus, W. H. 2020, ApJ, 897, 37
Oughton, S., Priest, E. R., & Matthaeus, W. H. 1994, JFM, 280, 95
Politano, H., & Pouquet, A. 1998, GeoRL, 25, 273
Schekochihin, A. A. 2022, JPlPh, 88, 155880501
Shebalin, J. V., Matthaeus, W. H., & Montgomery, D. 1983, JPlPh, 29, 525
Sorriso-Valvo, L., Marino, R., Carbone, V., et al. 2007, PhRvL, 99, 115001
Stone, J. M., Tomida, K., White, C. J., & Felker, K. G. 2020, ApJS, 249, 4
Taylor, M. A., Kurien, S., & Eyink, G. L. 2003, PhRvE, 68, 026310
Yang, Y., Linkmann, M., Biferale, L., & Wan, M. 2021, ApJ, 909, 175
Yang, Y., Matthaeus, W. H., Roy, S., et al. 2022, ApJ, 929, 142
Yang, Y., Shi, Y., Wan, M., Matthaeus, W. H., & Chen, S. 2016, PhRvE, 93, 061102
Zank, G., & Matthaeus, W. 1992, JGR, 97, 17189
Zank, G. P., & Matthaeus, W. 1993, PhFlA, 5, 257